

Detection of the phase curve and occultation of WASP-100b with *TESS*

Tiffany Jansen^{1*} and David Kipping^{1,2}

¹*Dept. of Astronomy, Columbia University, 550 W 120th Street, New York NY 10027*

²*Flatiron Institute, 162 5th Av., New York, NY 10010*

Accepted by MNRAS March 19, 2020

ABSTRACT

We report the detection of the full orbital phase curve and occultation of the hot-Jupiter WASP-100b using *TESS* photometry. The phase curve is isolated by suppressing low frequency stellar and instrumental modes using both a non-parametric harmonic notch filter (*phasma*) and semi-sector long polynomials. This yields a phase curve signal of (73 ± 9) ppm amplitude, preferred over a null-model by $\Delta\text{BIC} = 25$, indicating very strong evidence for an observed effect. We recover the occultation event with a suite of five temporally localized tools, including Gaussian processes and cosine filtering. This allows us to infer an occultation depth of (100 ± 14) ppm, with an additional ± 16 ppm systematic error from the differences between methods. We regress a model including atmospheric reflection, emission, ellipsoidal variations and Doppler beaming to the combined phase curve and occultation data. This allows us to infer that WASP-100b has a geometric albedo of $A_g = 0.16^{+0.04}_{-0.03}$ in the *TESS* bandpass, with a maximum dayside brightness temperature of (2710 ± 100) K and a warm nightside temperature of (2380^{+170}_{-200}) K. Additionally, we find evidence that WASP-100b has a high thermal redistribution efficiency, manifesting as a substantial eastward hotspot offset of $(71^{+2}_{-4})^\circ$. These results present the first measurement of a thermal phase shift among the phase curves observed by *TESS* so far, and challenge the predicted efficiency of heat transport in the atmospheres of ultra-hot Jupiters.

Key words: eclipses — planets and satellites: detection — methods: numerical — stars: planetary systems

1 INTRODUCTION

Hidden within the light curve of a star hosting an exoplanet is the light from the planet itself, waxing and waning as it traverses its orbit, reflecting and re-radiating its star’s incident rays. Upon folding a light curve into a function of orbital phase, flux modulations due to the presence of an orbiting companion can become prominent above the noise. In addition to the waxing and waning of the planet’s atmospheric phase curve, there are sinusoidal signatures caused by the apparent change in surface area of the tidally distorted star and the Doppler beaming of its radiation as the star orbits its system’s center of mass. While these stellar signals are indicative of the star-planet mass ratio, the amplitude and symmetry of the planetary phase curve reveal important atmospheric characteristics of the planet in question, such as its albedo, thermal redistribution efficiency, day-to-night temperature contrast, or whether a significant atmosphere exists at all (e.g. Knutson et al. 2007; Hu et al.

2015; Kreidberg et al. 2019; Parmentier & Crossfield 2018 and references therein).

Due to their often bloated radii and proximity to their host stars, hot-Jupiters are excellent candidates for atmospheric characterization. WASP-100b is one such hot-Jupiter discovered transiting a ~ 6900 K F2 star with a radius of $R_P = (1.69 \pm 0.29) R_\oplus$ (Hellier et al. 2014). Observations of this system with the Euler/CORALIE spectrograph reveal an eccentricity consistent with zero, and together with the transit data give a mass of $M_P = (2.03 \pm 0.12) M_\oplus$ (Hellier et al. 2014). With an orbital period of 2.9 days and a semi-major axis of $a = 0.046$ AU reported by Hellier et al. (2014), WASP-100b is likely tidally locked in a synchronous orbit to its star (Guillot et al. 1996).

At the time of writing, the Transiting Exoplanet Survey Satellite (*TESS*) has completed the Southern-hemispherical half of its primary mission to survey the brightest stars for transiting exoplanets (Ricker et al. 2015), and is well into its second half of the mission to survey the northern hemisphere. Only a handful of full phase curves have been measured in the *TESS* data prior to this study (Shporer et al.

* E-mail: jansent@astro.columbia.edu

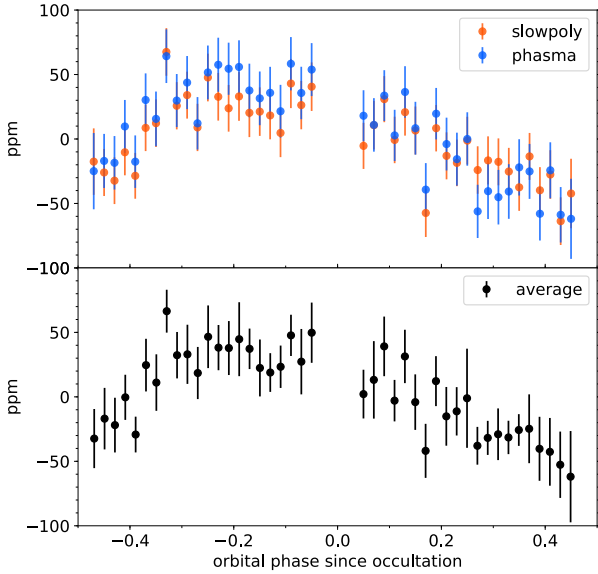


Figure 1. Phase curve of WASP-100 detrended by the polynomial method (top), the moving median method *phasma* (middle), and the average of the two (bottom) which is used in the analysis. The occultation and transit events at $x = 0.0, \pm 0.5$ have been removed both from this figure and before the regression analysis.

2019; Daylan et al. 2019; Bourrier et al. 2019; Wong et al. 2019). With an orbital period of 2.9 days, WASP-100b is the longest-period planet to have a full phase curve and occultation depth measured in the *TESS* data to-date. This is due in part to its location in the continuous viewing zone of the *TESS* field of view. By observing WASP-100 in each of the 13 observational sectors, we are able to increase the signal-to-noise ratio of WASP-100b’s phase curve by stacking 76 of its orbits.

In this study, we present the first occultation measurements of WASP-100b and aim to constrain its atmospheric characteristics such as albedo, thermal redistribution efficiency, intrinsic thermal scaling factor, and day-to-night temperature contrast. In Section 2, we describe our data processing methods, and in Section 3 we measure the occultation depth of WASP-100b. In Section 4, we describe the phase curve model used in our regression analysis, which is detailed in Section 5. The constraints we are able to place on the atmospheric characteristics of WASP-100b are presented in Section 6 and discussed in Section 7.

2 EXTRACTING THE PHASE CURVE

We analyze the 2-minute cadence Pre-search Data Conditioning simple aperture photometry (PDCSAP) light curves of the WASP-100 system (TIC 38846515, TOI 106) from *TESS* Sectors 1 – 13, downloaded from the Mikulski Archive for Space Telescopes on September 9th, 2019. All images were taken with *TESS* Camera 4. The PDCSAP light curves have been corrected for systematics with the Science Processing Operations Center pipeline (Jenkins et al. 2016).

Data with quality flags indicating any anomalous behavior were removed prior to analysis¹.

2.1 Outlier removal

We first remove any remaining outliers in the PDCSAP time series using a standard moving filtering approach. We evaluate a moving median smoothing function through the time series with a 10-point window, which we then linearly interpolate and evaluate the distance of the data away from this function. Points greater than $f\sigma$ away are classified as outliers, where σ is given by 1.4826 multiplied by the median absolute deviation of the residuals (a robust estimator of the standard deviation, Huber 1981), and f is set to 4. We choose 4-sigma on the basis that this results in an expectation that no more than one non-outlier data point will be erroneously removed, assuming Gaussian noise.

2.2 Nuisance signal detrending

We apply two methods for removal of long-term stellar variability and low frequency systematics. In order to correctly apply the methods described in the remainder of this section, it was necessary to first identify significant gaps of missing data in the light curve and concentrate on each continuous section of data individually for its reduction. We define a “significant” gap to be one which is greater than 10% of the moving median window. For both detrending methods this necessitates separating each sector of data at *TESS*’ data downlink gap, which lasts on the order of ~ 1 day in the middle of each sector’s baseline.

For the first method, we fit a low-order polynomial function to each semi-sector of the cleaned light curve using weighted linear least squares. The idea is that the polynomial acts as a low-cut filter, but in reality polynomials can present complex behaviour in the frequency domain. For each semi-sector, we mask the transits and then evaluate the Akaike Information Criterion (Akaike 1974) of the polynomial fit from 1st to 20th order. The preferred model (lowest AIC score) is adopted and used to normalize that semi-sector. This polynomial treatment is a fairly standard way of removing long term trends in phase curve analysis and has been used by previous studies of both *Kepler* and *TESS* data (e.g. Wong et al. 2020; Shporer et al. 2019).

We then separately apply *phasma*², a non-parametric moving median algorithm that operates as a harmonic notch filter with a kernel equal to the orbital period P , removing nuisance signals which are out of phase with the phase curve (e.g. long-term stellar variability and residual systematics). A mathematical description of this method can be found in Appendix A, and is further described in Section 2.2 of Jansen & Kipping (2018). Unlike the polynomial method, *phasma* not does assume any particular functional form for the nuisance signal, which leads to a generally less-precise but more-accurate detrending (Jansen & Kipping 2018).

The primary transit and occultation are removed prior

¹ Data quality flag descriptions can be found in Section 9 of the *TESS Science Data Products Description Document*.

² The development version of *phasma* can be downloaded at <https://github.com/tcjansen/phasma>

to the `phasma` detrending to avoid contaminating the moving median function and regression analysis. The semi-sector light curves are then stitched and phase folded, then binned into 500 points in phase using a weighted mean (where the weights come from the PDCSAP uncertainties). During this binning, we calculate new uncertainties for the binned points directly from the standard deviation of the data within that phase bin. In this way the errors are empirically derived. As apparent from Figure 1, the two methods produce very similar phase curves which provides confidence that the reconstructions are not purely an artefact of the algorithms used. For our regression analysis, we take the mean of the binned `phasma` detrended phase curve and the binned polynomial detrended phase curve to obtain the data which are modeled in Section 4.

2.3 Background contamination

According to The Exoplanet Follow-up Observing Program (ExoFOP) for *TESS* there are 10 other sources within 1 arcminute of WASP-100, the brightest at a separation of 28.1 arcseconds and about 13 times fainter than our target. With the *TESS* pixel width of 21 arcseconds, this source lies in an adjacent pixel to WASP-100. Additionally, WASP-100 shares its central pixel with another object at a separation of 3.78 arcseconds, which is about 400 times fainter than our target.

We correct for aperture contamination by background sources such as these by using these blend factors and following the prescription of Kipping & Tinetti (2010). Blend factors are obtained from the *TESS* crowding metric “CROWDSAP”, which is defined to be the ratio of the flux of the target to the total flux in the aperture³. The average crowding metric across all 13 sectors in which WASP-100 is observed is 0.93 ± 0.01 (i.e. a contamination of 7% in flux).

3 OCCULTATION

Formally, the `phasma` algorithm is not optimized for sharp features such as transits and occultations. This is because the convolution of a transit’s Fourier transform (characterized by harmonics of the transit duration (Waldmann et al. 2012)), with `phasma`’s harmonic notch filter (characterized by finite width notches) will, in general, lead to bleeding of the transit’s spectral power out of the notches, thereby distorting the transit profile (Jansen & Kipping 2018). For this reason, we elect to detrend the occultation data using a distinct approach from `phasma`.

Specifically, we follow the approach of Teachey & Kipping (2018) who detrend the photometry with a multitude of common algorithms to ensure the result is robust against detrending choices. We used CoFiAM (Kipping et al. 2013a), BIC-guided polynomial detrending to semi-sectors, BIC-guided polynomial detrending to local occultation regions, median filtering, and a Gaussian process. We choose local occultation regions spanning ± 2.5 transit durations from the time of occultation such that the baseline is larger than the

occultation window, but small enough to exclude a phase curve signature. After detrending the occultations, the signals were coherently phase-folded. The phase folded occultation resulting from each detrending method can be seen in Figure 2.

We find clear evidence for an occultation event at the expected location for a near-circular orbit for all five methods. The average depth of the occultation event is (100 ± 14) ppm with an additional systematic error of ± 16 ppm originating from the differences between the methods. The depth was obtained by regressing a Mandel & Agol (2002) transit model to the transit light curves, and then scaling that best fitting template light curve to the occultation event (with limb darkening turned off when applied to the occultation).

This formally assumes a circular orbit with a single free parameter describing the ratio of the transit-to-occultation depth ratio. To check that the orbital eccentricity is indeed consistent with a circular orbit, we allow the time of occultation to vary while fitting and measure a median offset of $t_{occ} = -120 \pm 329$ s, with an additional systematic error of ± 69 s across the five methods. This yields an upper limit on the eccentricity of $|e \cos \omega| < 0.0029$ to 3σ confidence (see Section 4.4.1 in Kipping 2011).

The weighted mean of the measured occultation depths is then used in our regression’s likelihood function in order to constrain the parameters contributing to the thermal component of the full phase curve.

4 OUT-OF-TRANSIT PHASE CURVE MODEL

We model the out-of-transit phase curve of the WASP-100 system as a sum of the planet’s atmospheric phase curve, photometric effects in-phase with the orbital period by the stellar host, and a constant term γ which accounts for possible residual noise from the detrending process,

$$\mathcal{F} = F_P(\phi, A_B, f, \epsilon) + F_\star(\phi, A_{\text{beam}}, A_{\text{ellip}}) + \gamma. \quad (1)$$

This expression gives the flux of WASP-100 normalized by the average flux of the star as a function of orbital phase ϕ . Here, we define the orbital phase as $\phi \equiv 2\pi(P^{-1}[t - t_0] + \frac{1}{2})$, where t_0 is the transit ephemeris and P is the orbital period. Note that this expression is shifted from the canonical definition of orbital phase by $\pi/2$ such that the transit occurs at $\phi = \pm\pi$ and the occultation occurs at $\phi = 0$. This is simply to maintain consistency with the model described in the remainder of this section.

The atmospheric contribution of the phase curve is described by a sum of the thermal component and the reflective component,

$$F_P(\phi, A_B, f, \epsilon) = F_T(\phi, A_B, f, \epsilon) + F_R(\phi, A_B). \quad (2)$$

We model the thermal component $F_T(\phi, A_B, f, \epsilon)$ with the Bond albedo A_B , a thermal redistribution efficiency factor ϵ (defined as in Cowan & Agol 2011a), and an intrinsic thermal scaling factor f . The thermal redistribution efficiency is here defined to be the ratio between the radiative timescale of the planet’s photosphere and the difference between the frequencies at which the photosphere rotates

³ CROWDSAP definition from the *TESS* Science Data Products Description Document.

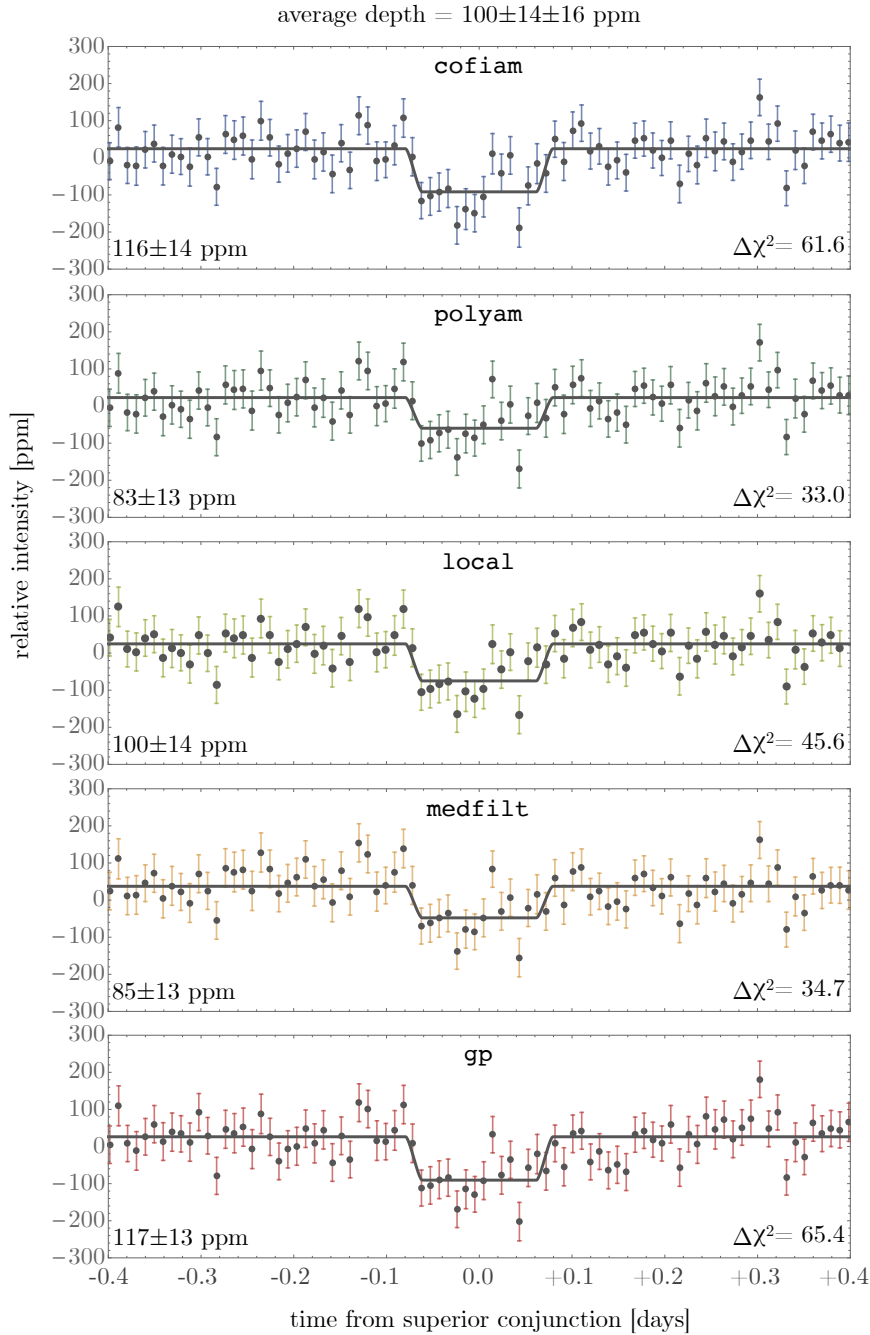


Figure 2. Comparison of the five different methods used to detrend the WASP-100b occultation events observed by *TESS*. We use the variability between the different methods to assign a ± 16 ppm “systematic” error on top of the ± 14 ppm random error.

about the planet and the surface rotates about its axis. In other words, if the atmospheric mass heated at the substellar point is redistributed about the surface much faster than the heat gets reradiated, the planet would be described as having a large redistribution efficiency ε , typically $\varepsilon \gg 1$. Conversely, a planet with relatively no heat redistribution would be described as having $\varepsilon = 0$. For a planet which has winds moving in a direction opposite of the planetary rotation, ε is defined to be negative. The intrinsic thermal factor f is simply a temperature scaling factor which accounts for any deviation from the equilibrium temperature due to e.g.

the presence of greenhouse gases in the atmosphere or interior heat from a dynamic core.

We express the thermal emission component of the phase curve as

$$F_T(\phi, A_B, f, \varepsilon) = \frac{1}{\pi B_{\tau, \star}} \left(\frac{R_P}{R_\star} \right)^2 \times \int_{-\frac{\pi}{2}}^{\frac{\pi}{2}} \int_{-\frac{\pi}{2}}^{\frac{\pi}{2}} B_{\tau, P}[T(\phi, \theta, \Phi)] \cos^2 \theta \cos \Phi d\theta d\Phi, \quad (3)$$

where $B_{\tau,\star}$ is the Planck function of the host star convolved with the wavelength response function of *TESS*⁴, R_P is the radius of the planet, R_\star the radius of the star, and $B_{\tau,P}[T(\phi, \theta, \Phi)]$ is the temperature distribution dependent blackbody curve of the planet convolved with the *TESS* bandpass,

$$B_{\tau,P}[T(\phi, \theta, \Phi)] = \int_{\lambda} \tau_{\lambda} \frac{2hc^2}{\lambda^5} \times \left[\exp\left(\frac{hc}{\lambda k_B T(\phi, \theta, \Phi)}\right) - 1 \right]^{-1} d\lambda \quad (4)$$

where τ_{λ} is the response function of *TESS*, and $T(\phi, \theta, \Phi)$ is the phase-dependent temperature distribution across the planet's surface, where ϕ , θ and Φ represent the orbital phase and planetary latitude and longitude as viewed in the observer's frame of reference, respectively. For our models we have chosen a surface resolution of $15^\circ \times 15^\circ$ in latitude and longitude, where further increasing the resolution only changes the thermal amplitude on the order of one-hundredth of a percent. It should be noted that Φ and θ are independent of phase, where $\Phi \equiv 0$ in the direction of the observer.

We borrow from [Hu et al. \(2015\)](#) to define the phase-dependent temperature distribution $T(\phi, \theta, \Phi)$ to be equal to

$$T(\phi, \theta, \Phi) = fT_0(\theta)\mathcal{P}(\varepsilon, \xi) \quad (5)$$

where T_0 is the sub-stellar temperature and \mathcal{P} is the thermal phase function, which for a planet on a circular orbit can be expressed by Equation (10) in [Cowan & Agol \(2011a\)](#):

$$\frac{d\mathcal{P}}{d\xi} = \frac{1}{\varepsilon} (\max(\cos \xi, 0) - \mathcal{P}^4) \quad (6)$$

where $\max(\cos \xi, 0) = \frac{1}{2}(\cos \xi + |\cos \xi|)$, i.e. a cosine function truncated at negative values. We borrow our notation from [Hu et al. \(2015\)](#), where ξ represents the local planetary longitude defined for all points in phase to be $\xi \equiv \Phi - \phi$ for a synchronously rotating planet. The phase term ϕ ranges from $-\pi$ to π and is defined to be zero at the occultation. For a planet with prograde rotation, $\xi = 0$ at the sub-stellar longitude, $\xi = -\pi/2$ at the dawn terminator, and $\xi = \pi/2$ at the dusk terminator.

Equation (6) does not have an analytic solution, so we solve it numerically using *scipy*'s ODE integrator, where we set the initial conditions equal to the approximated expression for $\mathcal{P}_{\text{dawn}}$ stated in the Appendix of [Cowan & Agol \(2011a\)](#),

$$\mathcal{P}_{\text{dawn}} \approx \left[\pi + (3\pi/\varepsilon)^{4/3} \right]^{-1/4}. \quad (7)$$

The sub-stellar temperature as a function of planetary latitude θ is expressed by

$$T_0(\theta) = T_\star \left(\frac{R_\star}{a} \right)^{1/2} (1 - A_B)^{1/4} \cos \theta^{1/4} \quad (8)$$

⁴ Approximately 600 - 1000 nm

where T_\star is the effective temperature of the host star and a the semi-major axis.

The reflection component of the atmospheric phase curve $F_R(\phi)$ is assumed to be symmetric, and is proportional to the geometric albedo A_g ,

$$F_R(\phi, A_B) = \left(\frac{R_P}{a} \right)^2 \frac{2}{3} A_B \frac{1}{\pi} [\sin|\phi| + (\pi - |\phi|) \cos|\phi|] \quad (9)$$

where we adopt the Lambertian approximation such that $A_g = \frac{2}{3}A_B$. According to [Seager et al. \(2000\)](#) and [Cahoy et al. \(2010\)](#), this is a fine approximation under the assumption that the atmosphere is reflecting homogeneously. Caveats of this assumption and the expectation of symmetry are discussed in Section 7.

The second term in Equation 1 describes the contribution to the phase curve by the host star,

$$F_\star(\phi, A_{\text{beam}}, A_{\text{ellip}}) = -A_{\text{beam}} \sin(\phi) - A_{\text{ellip}} \cos(2\phi). \quad (10)$$

The first sinusoidal term $A_{\text{beam}} \sin(\phi)$ accounts for relativistic beaming of the star's radiation as it orbits the system's center of mass ([Rybicki & Lightman 1979](#)). Ellipsoidal variations due to any tidal distortion of the host star by the close-in companion can be described by the second harmonic of the orbital period as $A_{\text{ellip}} \cos(2\phi)$ ([Morris 1985](#)). The amplitudes A_{beam} and A_{ellip} are left as free parameters in the regression and are described in further detail in Section 5.

The third term in our phase curve model γ accounts for a possible offset in the vertical alignment of our model from the data (not to be confused with the phase offset of the brightness maximum). Such an offset, which is constant in phase, could be a product of the normalization in the polynomial detrending process, an effect of *phasma*'s harmonic notch filter, or residual stellar noise (see Appendix A).

5 PHASE CURVE REGRESSION ANALYSIS

Bayesian inference of the model parameters, conditioned upon our phase curve data, is achieved using *emcee* ([Foreman-Mackey et al. 2013](#)). We allow the Bond albedo A_B , thermal redistribution efficiency ε , intrinsic thermal factor f , vertical adjustment term γ , scaled Doppler beaming amplitude $(A\alpha^{-1})_{\text{beam}}$, and scaled ellipsoidal variation amplitude $(A\alpha^{-1})_{\text{ellip}}$ to vary as free parameters. Although the scaling factors α_{beam} and α_{ellip} can be approximated analytically, we instead choose to leave them as free parameters to account for the uncertainty in their values. We obtain 10^6 samples from 2.5×10^4 steps across 40 walkers, burning the first half of the chains for a remaining total of 5×10^5 samples. The chains were inspected to ensure they had converged and achieved adequate mixing.

5.1 Transit fits

Many of the transit parameters affect the shape of the occultation and phase curve. For this reason, it is helpful to determine a-posteriori distributions for the transit terms, which can then serve as informative priors in the analysis of these effects. To this end, we detrended and regressed the *TESS*

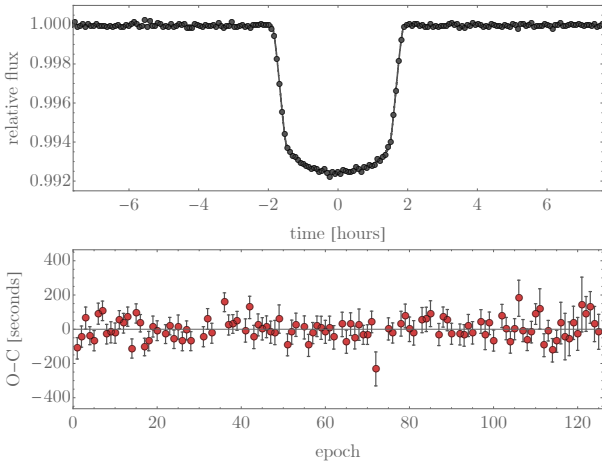


Figure 3. Top: Maximum a-posteriori light curve solution to the *TESS* data of WASP-100b. Here we show 13 sectors of photometry folded upon the best fitting ephemeris. Bottom: Transit timing variations of WASP-100b measured using *TESS*. We find no evidence for periodicity within the observed times.

data of WASP-100b’s transits for all thirteen available sectors. Detrending was performed by method marginalization over CoFiAM, a Gaussian process, a moving median filter, semi-sector polynomials, and epoch-localized polynomials. The resulting light curve was regressed using MULTINEST coupled to the Mandel & Agol (2002) forward transit model.

For these fits, we adopted uniform priors on the transit parameters, including the quadratic limb darkening coefficients re-parameterized to the q_1 - q_2 system (Kipping et al. 2013b). The only exception to this was for the stellar density, for which we adopt a Gaussian prior of $(440 \pm 100) \text{ kg m}^{-3}$, which comes from the isochrone analysis described in the following subsection (Section 5.2).

The maximum *a-posteriori* phase folded light curve model is shown in the top panel of Figure 3, which well describes the *TESS* data. The unbinned residuals to this solution display a standard deviation of 1227 ppm. The one-sigma *a-posteriori* credible intervals for the seven fitted parameters are given in Table 1.

To determine if there are any transit timing variations in the light curve of WASP-100, we fit the transits in each sector assuming global transit shape parameters and unique transit times. We find no evidence for any periodicity in the transit time residuals (see the bottom panel of Figure 3), which have a standard deviation of 65.1 seconds. Because the standard deviation of the residuals is very close to the median formal timing uncertainty of 64.3 seconds, we report there being no evidence for significant TTV signals.

5.2 Prior distributions

One useful piece of prior information in our analysis comes from the star itself. We elected to derive our own stellar parameter posteriors using an isochrone analysis of archival data. Specifically, we used T. Morton’s *isochrone* package (Morton 2015) with the Dartmouth stellar evolutionary models to constrain the host star’s fundamental parameters. For this analysis, we used $V = 10.8 \pm 0.06$ (Høg et al. 2000), $T_{\text{eff}} = 6900 \pm 120$, $[\text{Fe}/\text{H}] = -0.03 \pm 0.10$, $\log g = 4.35 \pm 0.17$

(Hellier et al. 2014) and the Gaia Data Release 2 parallax of $2.7153 \pm 0.0204 \text{ mas}$ (Gaia Collaboration et al. 2018). The resulting stellar parameters can be seen in Table 1.

For the atmospheric parameters A_B , ϵ , and f , we sample from uniform priors spanning $[0, 1]$, $[-10, 50]$, and $[1, 5]$, respectively. The vertical offset γ is sampled from a uniform prior spanning $[-200, 200]$ ppm. We can construct more informative priors for the mass-induced amplitudes A_{ellip} and A_{beam} from the spectroscopic radial velocity measurements of WASP-100 (Hellier et al. 2014) coupled with the posteriors of the transit light curve parameters and the characteristics of the host star modeled with *isochrones*, which can be seen in Table 1.

The scaled amplitude for the magnitude variation due to tidal distortion of the host star can be approximated as

$$(A\alpha^{-1})_{\text{ellip}} \approx K_{\text{RV}} \left(\frac{R_{\star}}{a} \right)^3 \frac{P}{2\pi a} \sin i, \quad (11)$$

where K_{RV} is the radial velocity semi-amplitude, R_{\star} the radius of the star, a the semimajor axis of the companion, P the orbital period, and i the inclination of the system in the observer’s line of sight. For this expression we used the approximations of Faigler & Mazeh (2011) and Morris & Naftilan (1993) on the theoretical derivations by Kopal (1959) and the momentum relation $m_p \sin(i) = M_{\star} K_{\text{RV}} P (2\pi a)^{-1}$. The scaling factor α_{ellip} contains the limb-darkening and gravity-darkening coefficients which we do not attempt to estimate, but instead leave as a free parameter with a uniform prior spanning the estimated range for F-G-K stars of $[1.0, 2.4]$ (Faigler & Mazeh 2011).

The beaming amplitude can be described by

$$(A\alpha^{-1})_{\text{beam}} = \frac{4K_{\text{RV}}}{c}. \quad (12)$$

where the scaling factor α_{beam} accounts for deviations from the beaming effect in a bolometric observation (the right side of Eq. 12) due to observing a spectrum that gets Doppler shifted within a finite bandpass (Loeb & Gaudi 2003; Faigler & Mazeh 2011). We adopt a conservative prior for α_{beam} , which we set to be uniform in the range $[0.5, 1.5]$.

The prior distributions for $(A\alpha^{-1})_{\text{ellip}}$ and $(A\alpha^{-1})_{\text{beam}}$ are then constructed from substituting 10^6 random samples from the posterior distributions of K_{RV} , R_{\star} , a , P , and i into Equations (11) & (12). The profiles of all prior distributions discussed in this section can be seen in Figure 4.

5.3 Likelihood function

The likelihood function describes how the data are distributed about the model. A typical approach is to detrend or whiten the data such that the likelihood function is simply a product of Gaussians. In this work, the data has indeed been partially whitened through a processing of photometric detrending. However, the detrending process applied to the phase curve is essentially a low-cut filter (i.e. removes low-frequency correlated noise components), and so leaves frequencies at or above the orbital frequency within the time series. This of course is necessary such that the phase curve signal is not removed, but it means that high frequency stellar noise, such as granulation, could persist in the light curve

Stellar parameters from isochrones fits	
T_{eff} (K)	6940 ± 120
R_* (R_\odot)	$1.67^{+0.18}_{-0.11}$
g (\log_{10} cm s $^{-2}$)	$4.16^{+0.06}_{-0.08}$
[Fe/H]	0.00 ± 0.08
M_* (M_\odot)	$1.47^{+0.06}_{-0.05}$
age (\log_{10} yr)	$9.18^{+0.09}_{-0.14}$
L_* ($\log_{10} L_\odot$)	$0.76^{+0.09}_{-0.05}$
d (pc)	368.2 ± 2.7
A_V	$0.15^{+0.23}_{-0.11}$
System parameters from transit fits	
P (days)	2.849382 ± 0.000002
ρ_* (kg m^{-3})	380^{+14}_{-13}
R_p/R_*	0.08683 ± 0.00037
b	$0.537^{+0.017}_{-0.020}$
t_0 (TJD)	1360.9376 ± 0.00001
q_1	$0.192^{+0.046}_{-0.039}$
q_2	$0.23^{+0.13}_{-0.10}$
Derived system parameters	
a (AU)	$0.043^{+0.005}_{-0.003}$
R_p (R_J)	$1.4^{+0.2}_{-0.1}$
i ($^\circ$)	84.4 ± 0.3
T_{eq} (K) †	2099 ± 38
From Hellier et al. (2014)	
M_p (M_{Jup})	2.03 ± 0.12
K_{rv} (km s^{-1})	0.213 ± 0.008
e	0 (< 0.10 at 3σ)

Table 1. System parameters for WASP-100 used in the regression analysis.

† For $A_B = 0$

and would be decidedly non-white. To remedy this, we work with the 500-point binned phase curve for our inference. Because each binned point spans ~ 76 orbital periods, high frequency noise on top of the orbital frequency will not - in general - be coherent, and thus will average out (Pont et al. 2006). This means that our phase curve data has not only had the low-frequency components suppressed, but the high frequency components too (by a factor of $\sqrt{76} \simeq 8.7$), which justifies our use of a Gaussian likelihood function in what follows.

For the occultation, rather than model the full occultation shape, the key piece of information is the actual depth. Further, since the depth has already been derived using an approach which includes systematic error from detrending differences, we elect to simply include the depth as a single datum in the likelihood function, along with its associated uncertainty. The likelihood function is then

$$\log \mathcal{L} = -\frac{n+1}{2} \log(2\pi) - \sum_{i=1}^n \log \sigma_i - \frac{1}{2} \sum_{i=1}^n \left(\frac{r_i}{\sigma_i} \right)^2 - \log \sigma_{occ} - \frac{1}{2} \left(\frac{r_{occ}}{\sigma_{occ}} \right)^2, \quad (13)$$

where n is the number of real-valued data points, σ_i the photometric uncertainty, and r_i the residuals of the phase curve model and the observed data.

The second line in Equation (13) describes the part of the likelihood function which takes the occultation depth measured in Section 3 into consideration when inferring the parameters of the phase curve model, where σ_{occ} is the uncertainty of the measured occultation depth and r_{occ} is the difference between a depth sampled randomly from its posterior distribution and the value of the model phase curve at the point in phase where the occultation occurs (i.e. $F(\phi = 0)$).

6 PHASE CURVE RESULTS

6.1 Occultation

The occultation depth of $(100 \pm 14 \pm 16)$ ppm is remarkably large and it is interesting to compare this result to theoretical expectation. We do this by evaluating the limiting case of a blackbody atmosphere (zero albedo) with no redistribution and completely efficient redistribution. Using the expressions of Cowan & Agol (2011b), we propagate our stellar and transit parameter posterior samples into their expressions for the day-side temperature (Eqn. 4) and then integrate over the *TESS* bandpass to predict $(26^{+3}_{-3} < \delta_{occ} < 128^{+11}_{-11})$ ppm. These extremes correspond to a disk-integrated day-side temperature of (2098 ± 37) K to (2680 ± 48) K. Accordingly, we conclude that our measured occultation depth is physically plausible, but towards the upper end of the scale. A complete interpretation is offered shortly in combination with the phase curve results.

6.2 Non-zero albedo

From our complete phase curve + occultation model, we show the marginalized posterior distributions of the model parameters as a corner plot in Figure 4. Of particular note is that the credible interval for the Bond albedo is $A_B = (0.24 \pm 0.06)$, apparently offset away from zero. For a Lambertian surface, this corresponds to a geometric albedo of $A_g = (0.16 \pm 0.04)$. The marginalized posterior density at $A_B = 0$ divided by the prior density yields the Savage-Dickey ratio (Dickey 1971), an estimate of the Bayes factor for a nested model. Here, we report a Bayes factor of 165 in very strong favor of a non-zero albedo.

6.3 Warm night side

The ratio between the radiative timescale and advective timescale of the atmospheric height probed by *TESS* is measured to be $\varepsilon = 10.9^{+5.3}_{-3.8}$, indicating heat transport from the substellar point to the nightside in an eastward direction, i.e. the same direction as the rotation of the surface assuming WASP-100b is on a prograde orbit. This redistribution of

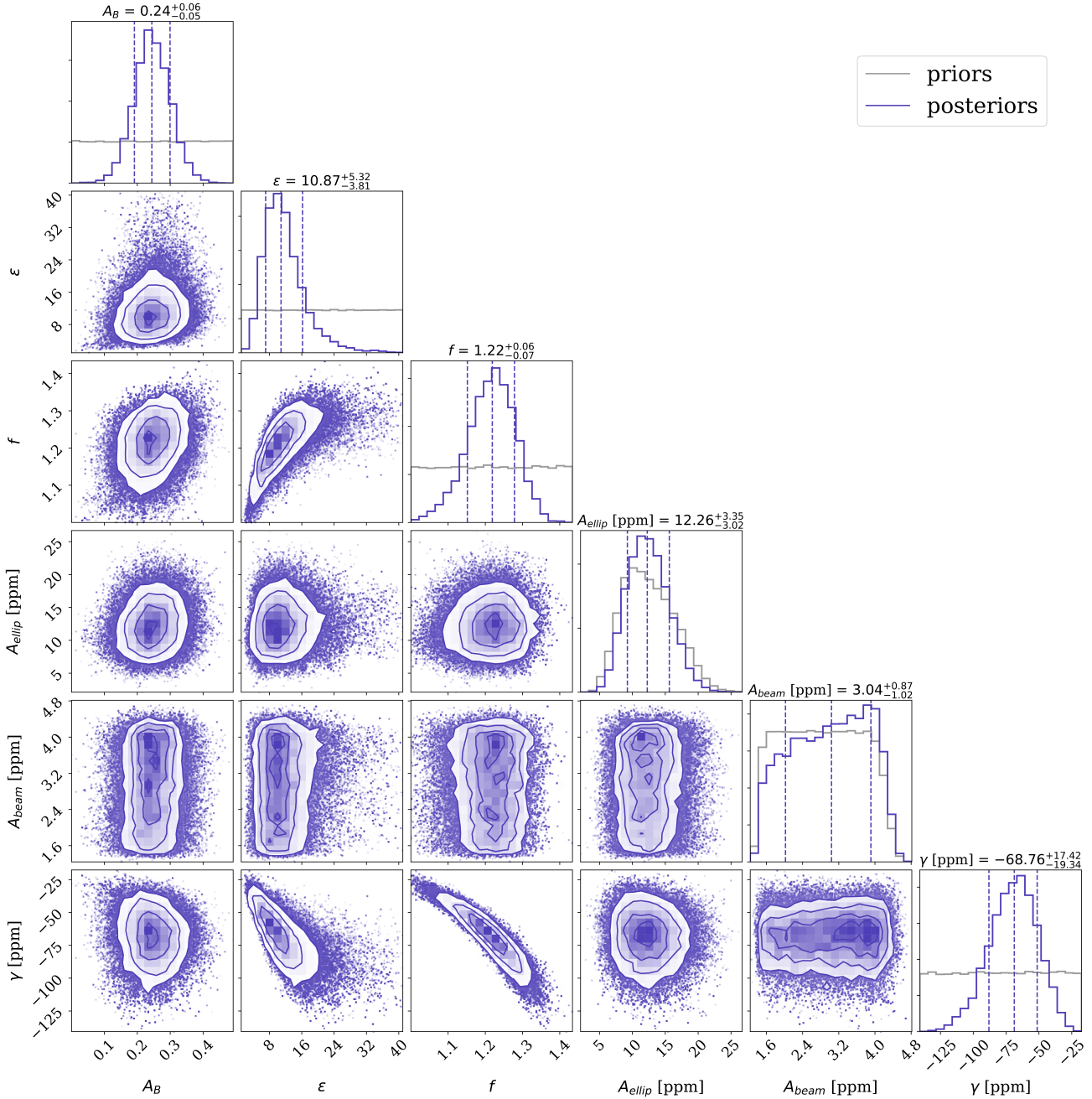


Figure 4. Points and histograms in purple show the posterior distributions for the Bond albedo A_B , thermal redistribution efficiency ϵ , intrinsic thermal scaling factor f , ellipsoidal variation amplitude A_{ellip} , relativistic beaming amplitude A_{beam} , and vertical offset γ in the model fit to the phase curve of the WASP-100 system. Grey histograms show the corresponding prior distributions used in the Bayesian regression analysis.

heat causes an eastward shift of the brightest region in the atmosphere of WASP-100b. Using the Savage-Dickey ratio to test the $\epsilon = 0$ case in which there is no thermal redistribution returns a Bayes factor of 151, which is in very strong favor of the model with efficient thermal redistribution. This result is supported by the fact that the occultation depth exceeds the peak-to-peak phase curve amplitude, implying a hot night side. It will be important to verify this result using

other observatories; additionally *TESS* Cycle 3, which will revisit the field hosting WASP-100.

6.4 Evidence for winds

We find that the phase of maximum brightness occurs $(63^{+6}_{-8})^\circ$ prior to the phase of occultation. However, the phase of maximum brightness in the observed phase curve seen in Figure 5 does not correlate to the phase shift of the atmo-

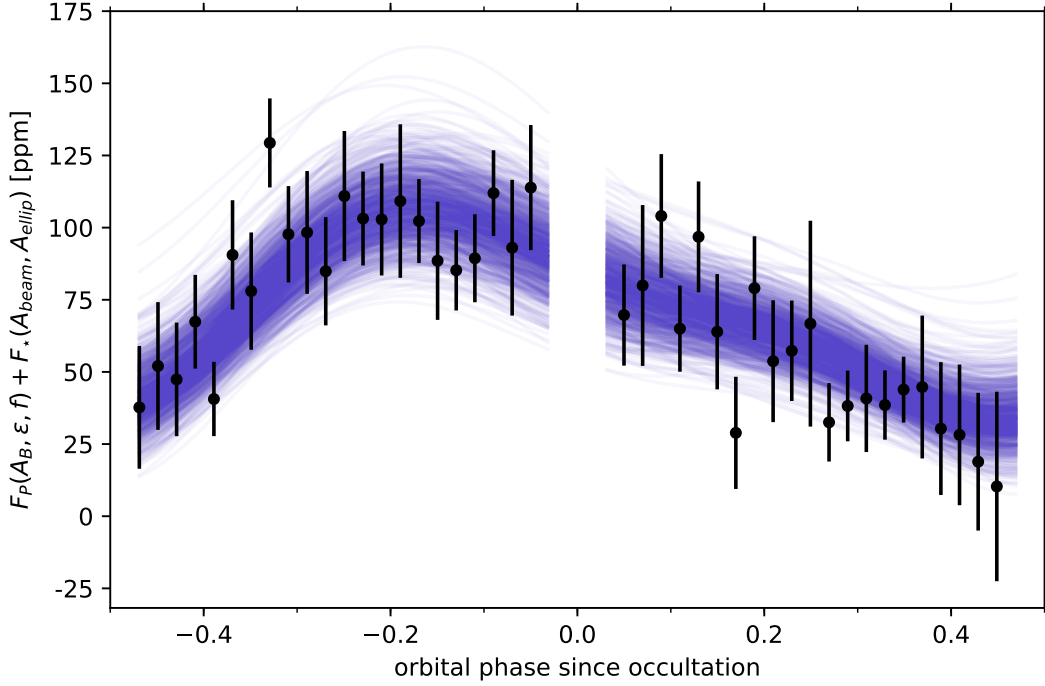


Figure 5. The normalized out-of-transit phase curve of the WASP-100 system averaged across observations made in sectors 1-13 of the *TESS* data (black points). Error bars are of the 1σ photometric uncertainties of the data binned into 43 points in phase. The purple lines show a range of phase curve models constructed from 1000 random samples in the posterior distributions from the regression analysis. Blank regions in the phase curve correspond to the occultation (at phase = 0) and transit (phase = ± 0.5), which are masked for analysis of the out-of-transit phase curve. The data have been shifted by the average γ value from the posteriors to align with the model samples.

Parameter	Value
A_B	$0.24^{+0.06}_{-0.05}$
A_g^\dagger	$0.16^{+0.04}_{-0.03}$
ϵ	$10.9^{+5.3}_{-3.8}$
f	$1.22^{+0.06}_{-0.07}$
T_{max} (K)	2710 ± 100
T_{min} (K)	2380^{+170}_{-200}
$T_{max} - T_{min}$ (K)	320^{+150}_{-100}
Thermal hotspot offset ($^\circ$ E)	71^{+2}_{-4}
Night-side flux at eclipse (ppm)	50^{+22}_{-19}
Atmospheric offset ($^\circ$)	28^{+9}_{-8}
Atmospheric amplitude ‡ (ppm)	62 ± 9
Max-brightness offset ($^\circ$)	63^{+6}_{-8}
Max-brightness amplitude ‡ (ppm)	73 ± 9

Table 2. Measured and derived values from the model fits to the phase curve of WASP-100b.

† With the assumption of a Lambertian atmosphere such that

$$A_g = \frac{2}{3}A_B$$

‡ Amplitude is peak-to-peak

spheric signal, since the observed phase curve is a convolution of the atmospheric phase curve and the coherent photometric effects of the star. This is illustrated in the bottom panel of Figure 6, which shows the observed phase curve

deconvolved into its stellar and atmospheric components according to samples from the regression analysis.

Additionally, because we measure a significant contribution of reflected light to the atmospheric phase curve, even the phase shift of the atmospheric component, measured to be $(28^{+9}_{-8})^\circ$, does not directly correlate to the offset of the hottest longitude from the substellar point (see the top panel of Figure 6). After deconvolving the thermal and reflected components of WASP-100b's phase curve, we measure a longitudinal hotspot offset of $(71^{+2}_{-4})^\circ$ east of the substellar point. We measure the brightness temperature of the hottest spot to be (2720 ± 150) K, where the temperature of the coolest spot is (2400 ± 220) K, giving a longitudinal temperature contrast of $\Delta T = (320^{+150}_{-100})$ K.

As a point of reference, we calculate the theoretical maximum peak temperature of WASP-100b using the expression for the temperature at the substellar point from Cowan & Agol (2011a) (Eqn. 4), assuming a zero albedo and no thermal redistribution. Leveraging our posterior samples from the transit and isochrone solution, we estimate that the expected maximum peak temperature should be no more than $T = (2967 \pm 53)$ K, which the credible interval of our maximum measured temperature is indeed below.

6.5 Additional heating?

The intrinsic thermal scaling factor f , which signifies a deviation from WASP-100b's equilibrium temperature, is mea-

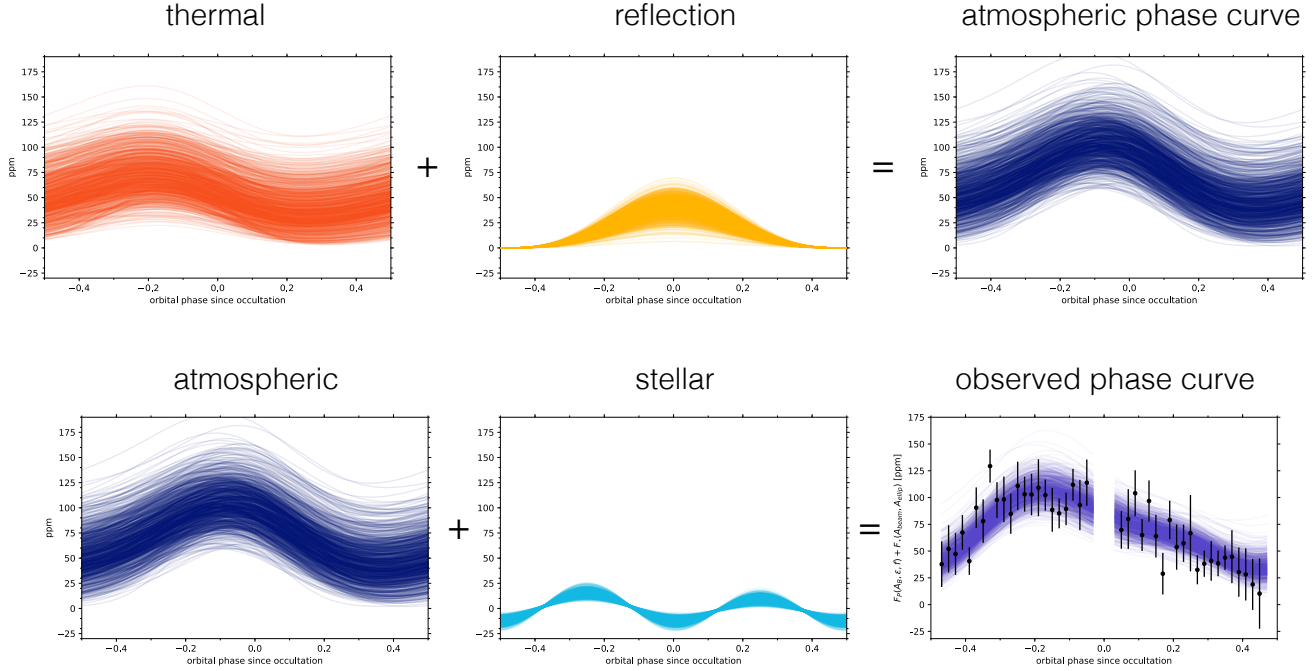


Figure 6. Samples from the posterior distribution of the model phase curve of the WASP-100 system deconvolved into the atmospheric components of WASP-100b’s phase curve (top) and the separate planet/host components (bottom). The atmospheric component includes both reflected light from the host star and thermal radiation from the planet itself. The phase of maximum brightness in the atmospheric phase curve is offset from where the planet would appear to be in full-phase due to thermal redistribution from the hot day side to the cooler night side, resulting in an eastward deviation of the hotspot from the substellar point.

sured to be $f = 1.22 \pm 0.07$. This suggests some modest evidence for additional heating from an internal source, but with a Bayes factor of only 3.9 compared to the $f = 1$ case, we caution that this result is somewhat marginal and cannot be verified using the independent occultation measurement on its own. Further, the theoretical maximum temperature is clearly above our inferred peak temperature, suggesting that no extra heating is needed. However, that calculation assumes zero albedo and our models favor a modest albedo which explains the behavior of the f factor inflating slightly above unity to compensate for that energy loss.

It is thus apparent that a slight degeneracy exists between a moderate- ϵ /moderate- f model and a greater- ϵ /greater- f model, which can be explained by the change in the phase curve amplitude with ϵ and the flexible nature of the model’s vertical baseline. When the thermal redistribution efficiency of the atmosphere is high, the air mass heated at the substellar longitude is redistributed toward the nonirradiated hemisphere in an attempt to reach thermodynamic equilibrium, which results in a phase-shifted “hot-spot,” and a diminished thermal amplitude due to the decrease in temperature contrast between the day and night sides. Consequently, the vertical baseline of the thermal phase curve will be greater for a more thermally redistributed atmosphere because the nightside has a higher temperature than one in which there is little to no thermal redistribution.

A model which fits well to the phase offset and amplitude of the data in Figure 5 can be constructed with a high thermal redistribution efficiency ϵ and intrinsic ther-

mal scalar f . However, the data can also be well represented by an even larger ϵ as long as f , and therefore the average temperature of WASP-100b, is also increased in order to maintain the thermal phase curve amplitude that is given by the out-of-transit data and measured occultation depth. When ϵ and f increase, the vertical baseline of the model shifts upward, and therefore the magnitude of the baseline correction also increases to minimize χ^2 . Once $\epsilon \gg 1$, further increasing the magnitude of ϵ has little affect on the phase offset of the point of maximum brightness.

6.6 Gravitational effects

We are unable to measure the Doppler beaming amplitude of WASP-100, though this is to be expected for an upper limit of < 4.2 ppm at 95% confidence on the amplitude of this signal. The data do not appear to put a significantly tighter constraint on the ellipsoidal variation amplitude compared to its prior distribution (Figure 4), which has an amplitude distribution of (12 ± 3) ppm. The posterior distribution of the ellipsoidal variation amplitude corresponds to a planetary mass of $1.97^{+0.48}_{-0.40} M_{\oplus}$, which is in agreement with the prior set by the mass measured by the radial velocity observations in [Hellier et al. \(2014\)](#).

6.7 Statistical significance

To gauge the statistical significance of our results, we conduct additional regression analyses for five simpler phase

Table 3. Model selection statistics on the phase curve of WASP-100b (binned into 439 points). The “full model” refers to Equation 1, while models labeled “full model – [component]” refer to model scenarios which do not include said component. Values correspond to the median models constructed from 1000 samples from their respective posterior distributions.

Models	χ^2	BIC	AIC
Flat line	452	458	454
Full model	385	434	401
Full model – beaming	385	421	397
Full model – ellipsoidal	391	428	403
Full model – reflection	390	439	406
Full model – thermal	409	446	421

Flat line model against the...	Δ BIC	Δ AIC
full model	24.7	53.2
full model – beaming	36.9	57.3
full model – ellipsoidal	30.8	51.2
full model – reflection	19.8	48.4
full model – thermal	12.8	33.2

curve models and compare their Bayesian information criteria (BIC, Schwarz 1978) and Akaike information criteria (AIC, Akaike 1974) to that of the full model which describes the atmospheric phase curve and the stellar contribution to the phase curve (Equation 1). Both criteria measure model likelihood while penalizing a higher number of free parameters.

The simplest model is that of the null result, which in this case is a flat line constant in phase. When comparing the likelihood of the fit to the full model to that of the null model, we compute Δ BIC = 25 in strong favor of the full phase curve model. The AIC is even less punitive toward the number of free parameters, for which we measure Δ AIC = 53 in very strong favor of the full model.

To judge whether the thermal and reflection components of the atmospheric phase curve are significantly retrieved, we repeat our regression analysis against models which exclude these atmospheric components, i.e. Equation 1 in the case that i) $F_P = F_R(\phi, A_B)$ and ii) $F_P = F_T(\phi, A_B, f, \epsilon)$. For the case in which the atmospheric phase curve is modeled by only a thermal component, Δ BIC = 6 in strong favor of the full model. The case in which the atmospheric phase curve is modeled only by reflection performs even more poorly, measuring Δ BIC = 13 in even stronger favor for the model which includes both atmospheric components.

We then perform additional regression analyses on a pair of models which do not include the stellar components of the phase curve, namely the Doppler beaming and ellipsoidal variation effects. The model excluding ellipsoidal variations is strongly preferred over the full model, with Δ BIC = 6. For the case in which $A_{\text{beam}} = 0$, Δ BIC = 6 compared to the model without ellipsoidal variations, and Δ BIC > 10 against all of the other models, which makes the phase curve model without Doppler beaming the most significantly preferred model of the six tested here.

From the statistical analysis discussed in this section, we conclude that the phase curve signal of WASP-100b is real and significant. The values for the BIC and AIC for each of the models tested in this section can be seen in Table 3.

6.8 Addressing the effect of TESS’s momentum dumps and other aspects of data reduction

The reaction wheels on the TESS spacecraft experience a build up of momentum which is corrected for by resetting the reaction wheel speeds to lower values approximately once every 2.5 days, where each momentum dump causes a momentary increase in the spacecraft’s pointing instability⁵. The occurrence rate of these momentum dumps is close enough to the orbital period of the planet (~ 2.8 days) to elicit some concern for the potential effect this may have on WASP-100b’s phase curve.

To measure the magnitude of this effect, we construct a model of the momentum dump profile in phase with WASP-100b and measure its maximum peak-to-peak amplitude. To do this, we first locate the time of each momentum dump in all sectors of WASP-100’s observation and fold the detrended light curve as a function of time since the momentum dump. We then construct a model for the momentum dump profile by fitting a suite of polynomial functions of 0th to 20th order using weighted linear least squares, and select the polynomial which produces the lowest Akaike Information Criterion. We then unfold the noise-less polynomial model back into a function of time, and refold into phase with WASP-100b. The resulting profile has a maximum peak-to-peak amplitude significantly less than the peak-to-peak amplitude of the phase curve of WASP-100b, and is less than its 2σ error (74 ± 10 ppm). This analysis was repeated for both the `phasma` detrended light curve and the `slowpoly` detrended light curve, and for momentum dump models chosen by the Bayesian Information Criterion, each case showing the same result. From this we conclude that the momentum dumps of the spacecraft’s reaction wheels have an insignificant effect on the phase curve of WASP-100b.

Additionally, because each sector of observation comes with its own anomalies, we examine the effect each sector has on the binned phase curve of WASP-100b by removing one sector from the time series and comparing the resulting phase curve to the full 13-sector phase curve used in our analysis. In each case, the binned data are all well within the 2σ error of the binned data in the full phase curve, indicating that no one sector is significantly affecting the profile of the phase curve of WASP-100b.

To examine if our choice of binning statistic has an effect on the results presented in the previous sections, we repeat the regression analysis for the phase curve constructed with median binning, and find that all results presented in Table 2 agree within 1σ significance.

7 DISCUSSION

The results presented in this paper suggest that the atmosphere of WASP-100b is likely to have a strong thermal redistribution efficiency indicative of atmospheric winds, with significant reflectivity in the TESS waveband. From the measured occultation depth and regression analysis of the phase curve, we measure a maximum dayside temperature of 2720 ± 150 K, placing WASP-100b in the “ultra hot” class

⁵ See the [TESS Data Release Notes](#)

of Jupiter-sized exoplanets (Parmentier et al. 2018; Arcangeli et al. 2018; Bell & Cowan 2018). Our study provides more insight into this relatively new class of exoplanets.

7.1 WASP-100b in context

Of the three hot-Jupiter phase curves which have been observed by *TESS* so far (Shporer et al. 2019; Daylan et al. 2019; Bourrier et al. 2019; Wong et al. 2019), WASP-100b is the first to show a thermal phase shift indicative of efficient heat transport in its atmosphere. The magnitude of its $71 \pm 4^\circ$ hotspot offset is rivaled only by the phase shift of υ Andromedae b, which has been measured to be $(84.5 \pm 2.3)^\circ$ (Crossfield et al. 2010). Such a large thermal phase shift is unexpected for ultra-hot Jupiters such as WASP-100b, which have been predicted to have much shorter radiative time scales than thermal redistribution time scales, and therefore negligible phase curve offsets (Perez-Becker & Showman 2013; Komacek & Showman 2016; Komacek et al. 2017; Schwartz et al. 2017). The eastward direction of WASP-100b’s hotspot offset is, however, typical of hot-Jupiters which have been previously observed to have asymmetric thermal phase curves (Parmentier & Crossfield 2018 and references therein).

Bell & Cowan (2018) have recently suggested a possible mechanism for increased heat transport specific to ultra-hot Jupiters, which may help explain WASP-100b’s unexpectedly large eastward hotspot offset. On the day sides of these worlds, temperatures are hot enough to dissociate hydrogen molecules. This hydrogen gas is then carried by eastward winds from the sub-stellar point to cooler longitudes, where temperatures are low enough to allow for the recombination of H_2 . This recombination is a highly exothermic process, releasing a significant amount of energy via latent heat to the surrounding gas. On the opposite hemisphere, the recombined molecular gas is carried back to the hotter day side, where latent heat is used in the redissociation of H_2 , effectively cooling the longitudes west of the sub-stellar point.

Indeed, when Komacek & Tan (2018) included heat transport via H_2 dissociation/recombination in a follow-up study to Komacek & Showman (2016), they found that the day-night temperature contrast of ultra-hot Jupiters decreased with increasing incident stellar flux, the opposite conclusion of their previous theoretical analysis. A quantitative analysis of the significance of H_2 dissociation/recombination in the heat recirculation of WASP-100b is a bit beyond the scope of this study, although we acknowledge it would certainly be worth exploring.

Our ability to measure such a large shift in the phase curve of WASP-100b may be a product of the long observational baseline of the WASP-100 system. A majority of the planets viewed by *TESS* can only be observed for a maximum of 27 days, i.e. the duration of one observational sector in the *TESS* mission. For planets with peak-to-peak phase curve amplitudes as low as WASP-100b’s (Table 2), the majority will not have enough data to detect a phase curve with a significant signal to noise ratio. The convenient location of WASP-100 in the continuous viewing zone of *TESS* has allowed its observation through many orbits, therefore strengthening the signal to noise ratio of a phase curve amplitude which is relatively small due to the decreased longitudinal temperature contrast of WASP-100b.

WASP-100b’s geometric albedo of 0.17 ± 0.05 is among the highest measured from a *TESS* phase curve so far, comparable to the geometric albedo of WASP-19b (Wong et al. 2019) and significantly greater than that measured of WASP-18b (Shporer et al. 2019) and WASP-121b (Daylan et al. 2019). The albedo we measure is in line with the expectation for hot-Jupiters to have a relatively low reflectivity in the optical to near-infrared transition regime (Mallonn et al. 2019) and is similar to that of several hot-Jupiters observed by *Kepler* (Angerhausen et al. 2015).

7.2 Caveats

In modeling the phase curve of a star-planet system, there is some danger in confusing a star’s relativistic beaming signal for an eastward offset of the hotspot in the planet’s atmospheric phase curve. Fortunately we are able to break this degeneracy for the WASP-100 system with the radial velocity measurements presented in Hellier et al. (2014) (see Table 1), which we use to construct an informative prior on the magnitude of the star’s relativistic beaming amplitude in our regression analysis.

The main limitations of our atmospheric phase curve model lie in are our assumptions that the atmosphere of WASP-100b is Lambertian, and radiates as a blackbody. If the atmosphere of WASP-100b is in actuality composed of many particles that scatter photons in a preferential direction, the relative contributions of the modeled reflection and thermal components to the observed phase curve would have to be altered accordingly (Dyudina et al. 2005). Approximating WASP-100b’s spectrum as that of a blackbody could be an adequate model for the dayside spectrum, where temperatures are high enough to dissociate absorbent molecules such as H_2O , TiO , and VO , and to support a H^- continuum opacity (Arcangeli et al. 2018; Lothringer et al. 2018). Because we measure a high redistribution efficiency of heat from the day side to the night side on WASP-100b, the 2400 ± 200 K nightside temperature we derive from the model fit may also be high enough to justify the blackbody approximation, although the posterior distribution of this measurement indicates the nightside temperature is likely low enough to maintain the molecular bond of prominent visible-infrared absorbers such as titanium oxide and vanadium oxide (Lothringer et al. 2018), in which case the blackbody assumption would not hold.

ACKNOWLEDGMENTS

This paper includes data collected by the *TESS* mission, which are publicly available from the Mikulski Archive for Space Telescopes (MAST). Funding for the *TESS* mission is provided by the NASA Explorer Program. This research has made use of the `corner.py` code and `emcee` package by Dan Foreman-Mackey at github.com/dfm/corner.py and github.com/dfm/emcee, `scipy`, `astropy`, and the NASA Exoplanet Archive, which is operated by the California Institute of Technology, under contract with the National Aeronautics and Space Administration under the Exoplanet Exploration Program. We would also like to thank Ian Wong and Avi Shporer for their helpful correspondence and insight.

REFERENCES

- Akaike H., 1974, *IEEE Trans. Autom. Control*, 19, 716
- Angerhausen, D., DeLarme, E. & Morse, J. A., 2015, *ApJ*, 127, 1113
- Arcangeli J., et al., 2018, *ApJL*, 855, L30
- Bell T. J., Cowan N. B., 2018, *ApJL*, 857, L20
- Bourrier, V., Kitzmann, D., Kuntzer, T., et al. 2019, *A&A*, in revision, arXiv:1909.03010
- Cahoy, K. L., Marley, M. S. & Fortney, J. J. 2010, *ApJ*, 724, 189
- Cowan, N. B., & Agol, E. 2011a, *ApJ*, 726, 82
- Cowan, N. B., & Agol, E. 2011b, *ApJ*, 729, 54
- Crossfield I. J. M., Hansen B. M. S., Harrington J., Cho J. Y.-K., Deming D., Menou K., Seager S., 2010, *ApJ*, 723, 1436
- Daylan, T., Günther, M. N., Mikal-Evans, T., et al. 2019, *AJ*, in revision, arXiv:1909.03000
- Dickey J. M., 1971, *Ann. Math. Statist.* 42, 204
- Dyudina, U. A., Sackett, P. D., Bayliss, D. D. R., et al. 2005, *ApJ*, 618, 973
- Faigler, S. & Mazeh, T. 2011, *MNRAS*, 415, 3921
- Foreman-Mackey D., Hogg D. W., Lang D., Goodman J., 2013, *PASP*, 125, 306
- Gaia Collaboration et al., 2018, *A&A*, 616, A1
- Guillot T., Burrows A., Hubbard W., Lunine J., Saumon D., 1996, *ApJL*, 459, L35
- Hellier C., et al., 2014, *MNRAS*, 440, 1982
- Høg E., et al., 2000, *A&A*, 355, L27
- Hu R., Demory B.-O., Seager S., Lewis N., Showman A. P., 2015, *ApJ*, 802, 51
- Huber, P. J. 1981, *Robust Statistics*. New York: John Wiley and Sons
- Jansen, T., & Kipping, D. M. 2018, *MNRAS*, 478, 3025
- Jenkins 2016, *Proc. SPIE 9913*, Software and Cyberinfrastructure for Astronomy IV, 99133E
- Kipping, D. M., & Tinetti, G. 2010, *MNRAS*, 407, 2589
- Kipping, D.M., 2011, *The Transits of Extrasolar Planets with Moons*, Springer, Berlin
- Kipping, D. M., Hartman, J., Buchhave, L. A., et al. 2013a, *ApJ*, 770, 101
- Kipping, D. M., 2013b, *MNRAS*, 435, 2152
- Komacek, T. D., & Showman, A. P. 2016, *ApJ*, 821, 16
- Komacek, T. D., Showman, A. P., & Tan, X. 2017, *ApJ*, 835, 198
- Komacek T. D., Tan X., 2018, *Research Notes of the American Astronomical Society*, 2, 36
- Kopal, Z. 1959, *Close binary systems*, The International Astrophysics Series (London: Chapman & Hall)
- Kreidberg, L. et al., 2019, *Nature*, 573, 87
- Knutson H. A., et al., 2007, *Nature*, 447, 183
- Loeb A., Gaudi S. B., 2003, *ApJ*, 588, 117
- Lothringer J. D., Barman T., Koskinen T., 2018, *ApJ*, 866, 27
- Mallon, M., Köhler, J., Alexoudi, X., et al. 2019, *A&A*, 624, A62
- Mandel K., Agol E., 2002, *ApJ*, 580, L171
- Morris S. L., 1985, *ApJ*, 295, 143
- Morris, S. L., & Naftilan, S. A. 1993, *ApJ*, 419, 344
- Morton T. D., 2015, *isochrones: Stellar model grid package*, Astrophysics Source Code Library (ascl:1503.010)
- Parmentier V., Crossfield I. J. M., 2018, *Exoplanet Phase Curves: Observations and Theory*. p. 116, doi:10.1007/978-3-319-55333-7116
- Parmentier V., et al., 2018, *A&A*, 617, A110
- Perez-Becker, D., & Showman, A. P. 2013, *ApJ*, 776, 134
- Pont F., Zucker S., Queloz D., 2006, *MNRAS*, 373, 231
- Ricker G. R. et al., 2015, *J. Astron. Telesc. Instrum. Syst.*, 1, 014003
- Rybicki G. B., Lightman A. P., 1979, *Radiative Processes in Astrophysics*. Wiley, New York
- Schwarz G. E., 1978, *Ann. Stat.*, 6, 461
- Schwartz J. C., Kashner Z., Jovmir D., Cowan N. B., 2017, *ApJ*,

- 850, 154
- Seager, S., Whitney, B. A., & Sasselov, D. D. 2000, *ApJ*, 540, 504
- Shporer A., et al., 2019, *AJ*, 157, 178
- Teachey, A. & Kipping, D., 2018, *Science Advances*, 4, 1784
- Waldmann, I. P., Tinetti, G., Drossart, P., et al. 2012, *ApJ*, 744, 35
- Wong, I., et al., accepted for publication, *AJ*, arXiv:1912.06773
- Wong, I., et al., 2020, *AJ*, 159, 29

APPENDIX A: NON-PARAMETRIC DETRENDING WITH PHASMA

In Jansen & Kipping (2018), we state that the final phase curve function we want can be expressed as

$$\begin{aligned}\tilde{F}(t) &= \frac{F_P(t)}{F_\star} \\ &= \frac{F(t) - G(t)}{G(t)}\end{aligned}\quad (\text{A1})$$

where $F(t)$ is the observed light curve, i.e. $F(t) = F_P(t) + F_\star(t)$, and $G(t)$ is the “nuisance” function defined by

$$G(t) = \overline{F_P} + \Pi(t) * F_\star(t)$$

where

$$\Pi(t) = \begin{cases} 1 & \text{for } t - \frac{P}{2} < t < t + \frac{P}{2} \\ 0 & \text{else} \end{cases}.$$

In other words, $G(t)$ is a moving mean function with window = P . The stellar flux $F_\star(t)$ can also be expressed by a sum of some low frequency oscillations (where we define “low” to mean frequencies much less than the planet’s orbital frequency) due to e.g. spots on the surface of a slow rotator, and much higher frequency residuals about this low frequency mean:

$$F_\star(t) = F_{\star,low}(t) + \Delta F_\star(t). \quad (\text{A2})$$

Our first assumption is that the residuals about the lower frequency stellar signal are approximately equally mixed between positive and negative values, in which case their sum about the mean converges on zero. Therefore $G(t)$ is reduced to

$$G(t) = \overline{F_P} + F_{\star,low}(t) \quad (\text{A3})$$

Substituting the above back into Equation A1, we get

$$\begin{aligned}\tilde{F}(t) &= \frac{F_P(t) + F_\star(t) - [\overline{F_P} + F_{\star,low}(t)]}{\overline{F_P} + F_{\star,low}(t)} \\ &= \frac{F_P(t) + F_\star(t)}{\overline{F_P} + F_{\star,low}(t)} - 1.\end{aligned}\quad (\text{A4})$$

If we make a second assumption that $\overline{F_P} \ll F_{\star,low}(t)$, Equation A4 becomes

$$\tilde{F}(t) = \frac{F_P(t)}{F_{\star,low}(t)} + \frac{F_{\star,low}(t) + \Delta F_\star(t)}{F_{\star,low}(t)} - 1. \quad (\text{A5})$$

Folding $\tilde{F}(t)$ about the exact period of the planet, the average of $\Delta F_\star(t)$ approaches zero as a consequence of our first assumption (although we account for any residual noise as a constant nonetheless), and $F_{\star,low}(t)$ averages to $\overline{F_{\star,low}}$. If

$\Delta F_*(t)$ averages to zero upon a phase fold, then from Equation A2 it should be true that $\overline{F_{*,low}} \approx \overline{F_*}$. Thus we get

$$\begin{aligned} \text{fold}_P(\tilde{F}(t)) &= \text{fold}_P\left(\frac{F_P(t)}{F_{*,low}(t)} + \frac{F_{*,low}(t) + \Delta F_*(t)}{F_{*,low}(t)} - 1\right) \\ &\approx \text{fold}_P\left(\frac{F_P(t)}{F_{*,low}(t)}\right) + \frac{\overline{F_{*,low}}}{\overline{F_{*,low}}} + \gamma - 1 \\ &\approx \frac{F_P(\phi)}{\overline{F_*}} + \gamma, \end{aligned} \quad (\text{A6})$$

the desired function plus a possible vertical offset γ , a constant which is left as a free parameter in our model fitting.

This paper has been typeset from a $\text{\TeX}/\text{\LaTeX}$ file prepared by the author.